JOURNAL OF GEOPHYSICAL RESEARCH, VOL. 104, NO. A10, PAGES 22,591–22,604, OCTOBER 1, 1999

Coherent HF radar backscatter characteristics associated with auroral forms identified by incoherent radar techniques: A comparison of CUTLASS and EISCAT observations

S. E. Milan, J. A. Davies, and M. Lester
Department of Physics and Astronomy, Leicester University, Leicester, England, United Kingdom

Abstract. Backscatter from decameter-wavelength field-aligned *F* region irregularities, as measured by the Cooperative UK Twin Located Auroral Sounding System (CUTLASS) Finland HF coherent radar, is compared with common volume plasma parameters and the electric field deduced by the European Incoherent Scatter (EISCAT) UHF incoherent radar system, for a 12 hour period from June 18 to June 19, 1996. During this interval we find an excellent agreement between irregularity Doppler velocity and bulk ion drift resolved along the CUTLASS beam. Backscatter is found to exist only in regions of nonzero electric field, as the **E**×**B** instability growth rate is dependent on *E*. Following a substorm expansion phase onset, backscatter largely disappears for a period of several hours, thought to be a consequence of nondeviative absorption of the HF radio wave in the *D* region or a quenching of the *F* region instability mechanism by enhanced *E* region Pedersen conductivity. Finally, the presence of auroral arcs within the scatter volume increases the intensity of backscatter returns and introduces a subsidiary peak, displaced from the preexisting peak, in the backscatter spectra; this subsidiary peak results in an increase in the apparent spectral width of the backscatter. We show how this allows the location of precipitation features within the field of view to be determined.

1. Introduction

The SuperDARN (Super Dual Auroral Radar Network) coherent HF radars [*Greenwald et al.*, 1995] are an important tool for the study of ionospheric convection under the influence of the magnetospheric electric field over large portions of the northern and southern high-latitude regions. Each radar has a field of view which covers some 4×10^6 km^2, but, unfortunately backscatter is not regularly observed over more than a relatively small proportion of the whole viewing area. The reason for this is twofold. On one hand, the nature of HF radio propagation is such that the ionosphere is not uniformly "illuminated" by the radar. On the other hand, ionospheric field-aligned density perturbations or irregularities, the targets from which HF radars scatter, are not necessarily present throughout the entire high-latitude ionosphere. Hence the boundary of a region of backscatter can correspond either to the edge of a region of irregularity generation or to the edge of a region of illumination of the ionosphere by the radar. In the former case, this boundary is of geophysical significance; in the latter, it is not. These two factors have been discussed at some length by *Milan et al.* [1997b, 1998]. That the edges of regions of backscatter can correspond to the ionospheric projection of magnetospheric boundaries has previously been demonstrated by *Rodger et al.* [1995] and *Milan et al.* [1999] by comparison of radar and optical aurora in the cusp region. An understanding of the plasma conditions under which ionospheric irregularities are generated is essential for assessing which of these two factors is the cause of an absence of backscatter in a particular portion of the field of view at any one time. As a corollary, this knowledge may allow geophysical conclusions to be reached about regions where radar aurora are absent, hence extending the amount of "useful" measurements made by the radar. In a related aspect, in regions where radar aurora are present, the physical mechanisms which control the intensity or spectral width of the backscatter spectra are not fully understood; though again, such knowledge could extend the information that can be derived from coherent radar observations.

In contrast to coherent radars, incoherent scatter radars can deduce a complete altitude profile of a variety of ionospheric plasma parameters, including electron density, ion and electron temperature, line-of-sight ion drift, etc., but only along a narrow beam. In the case of the tristatic European Incoherent Scatter (EISCAT) radar UHF facility located in northern Scandinavia, a complete three-component ion velocity vector can be measured. It is clear that a combination of these two observational techniques, incoherent and coherent scatter, could indeed be a powerful tool for the investigation of many geophysical phenomena.

The EISCAT radar is located within the field of view of the Cooperative UK Twin Located Auroral Sounding System (CUTLASS) Finland radar, the easternmost station of the present Northern Hemisphere SuperDARN chain. This presents an excellent opportunity for a comparison of UHF incoherent radar and HF coherent radar measurements. Such studies have been undertaken previously [e.g., *Villain et al.*, 1985; *Ruohoniemi et al.*, 1987; *Eglitis et al.*, 1998; *Davies et al.*, 1999], though generally to compare the drift velocity of *F* region ionospheric irregularities with the *F* region bulk ion drift velocity. The present paper extends upon these studies by comparing the power and spectral width of CUTLASS Finland radar backscatter spectra with the plasma parameters deduced by the EISCAT radar. The interval of study is 1800 UT, June 18, 1996, to 0600 UT, June 19, 1996, an interval previously discussed by *Davies et al.* [1999], during which was demonstrated an excellent correspondence between

Paper number 1999JA900277.
0148-0227/99/1999JA900277$09.00

the incoherent and coherent radar estimates of the convection electric field. The intention of this paper is not to investigate the large-scale geophysical processes occurring during this interesting interval, which will be the subject of a forthcoming study, but rather to determine the small-scale plasma and electric field conditions which give rise to targets for coherent HF radars.

To aid discussion in section 4, a brief description is given of the two basic interchange instabilities which give rise to field-aligned electron density perturbations in the F region ionosphere: the $\mathbf{E}\times\mathbf{B}$ or gradient drift instability and the current convective instability. A more comprehensive description can be found in the work of *Tsunoda* [1988, and references therein]. The $\mathbf{E}\times\mathbf{B}$ instability acts in the presence of a background electron density gradient with a component perpendicular to $\mathbf{B}$ and with an applied electric field $\mathbf{E}$ which has a component along the gradient. In the one-dimensional linear case the growth rate of this instability is given by $\gamma = V_0/L$ for $\omega << \nu_{in}$ [*Linson and Workman*, 1970] and $\gamma = (V_0\nu_{in}/L)^{1/2}$ for $\omega >> \nu_{in}$ [*Ossakow et al.*, 1978]; here V_0 is the background plasma drift velocity relative to the neutral atmosphere (assuming zero neutral winds, $V_0 = E/B$), L is the effective scale length of the electron density gradient perpendicular to $\mathbf{B}$, ν_{in} is the ion-neutral collision frequency, and ω ($\equiv \omega_r + i\gamma$) is the wave frequency. In general, L is defined as $L = k_\perp BN_e/[\mathbf{k}\cdot(\nabla N_e\times\mathbf{B})]$, where $\mathbf{k}$ is the irregularity wave vector. The electron density gradient can be in the horizontal or vertical directions; though as $\mathbf{B}$ is directed almost vertically at high latitudes, any vertical electron density gradient would have to be large for L to become significant. At F region altitudes it is thought that horizontal gradients are most important for irregularity generation. These background electron density gradients in which the $\mathbf{E}\times\mathbf{B}$ instability can grow are produced by large-scale structuring of the ionospheric plasma, for instance, by particle precipitation in the auroral zone or through convection processes [see *Tsunoda*, 1988].

The current convective instability is similar in nature to the $\mathbf{E}\times\mathbf{B}$ instability but grows in the presence of a field-aligned current, for example, auroral arcs, where γ is proportional to $V_\parallel$, the field-aligned drift velocity of electrons relative to ions [*Ossakow and Chaturvedi*, 1979].

2. Experimental Arrangement

As mentioned in section 1, this paper presents a comparison of backscatter observed by the CUTLASS Finland HF coherent scatter radar with plasma parameters measured by the EISCAT UHF incoherent scatter radar. Below we give a brief description of the experiment. For more information, the reader is directed to the work of *Greenwald et al.* [1995] and *Milan et al.* [1997b] for a detailed description of the CUTLASS system, to the work of *Milan et al.* [1997a] for a discussion of the interferometric technique that allows the elevation angle of arrival of backscatter returns to be determined, to the work of *Rishbeth and Williams* [1985] vis-à-vis the EISCAT tristatic system, and to the work of *Davies et al.* [1999] for a description of the combined CUTLASS-EISCAT experimental arrangement.

The CUTLASS Finland HF coherent scatter radar, located at Hankasalmi (62.3°N, 26.6°E), scans through sixteen azimuthal look directions, arranged symmetrically about the radar bore site of -12° (i.e. west of north), in each 2 min interval, with a dwell time in each beam of 7 s. Each sounding is gated into 75 range cells (here numbered 0-74) of 45 km in length, with a range to the first gate of 180 km. A seven-pulse scheme is transmitted, from which can be deduced a backscatter autocorrelation function (ACF), and hence spectrum, within each gate. In the standard processing, the power and spectral width of the backscatter are estimated by a functional fit (generally exponential) to the decorrelation of the ACF, and the Doppler velocity is estimated by a least-squares fit to the phase of the complex ACF. In the present study, the radar was transmitting at an operating frequency of 10 MHz and hence was sensitive to ionospheric irregularities with a wavelength of 15 m. It should be noted at this point that between 1800 and 1900 UT of the interval of interest, severe HF interference was experienced, reducing the sensitivity of the system.

The EISCAT UHF incoherent scatter radar consists of three parabolic dish antennas, one sited at Tromsø, Norway, with both transmit and receive capabilities, and two remote site receivers at Kiruna, Sweden, and Sodankylä, Finland. The system operates near 931 MHz. In the CP-1-K mode, employed during the present interval, the transmit beam is aligned along the local F region magnetic field. The remote site radars intersect the transmit beam at a single F region altitude, at which tristatic measurements of the ion drift are made; this intersection point is colocated with range gate 16 of beam 5 of the CUTLASS Finland radar. Four pulse schemes are transmitted: long pulse which gives F region measurements with an altitude resolution of 22 km; alternating code, which achieves an altitude resolution of 3.1 km at E region and lower F region altitudes; and two power profiles, which yield only return power measurements but from D region altitudes, at 3.1 and 4.5 km altitude resolutions. From the backscatter spectra several plasma parameters can be deduced, including electron density N_e and ion and electron temperatures T_i and T_e. Also, with the inclusion of a suitable collision frequency model, the Hall and Pedersen conductivities can be determined [see, e.g., *Davies and Lester*, 1999]. The EISCAT measurements have been post-integrated to a time resolution of 2 min to be comparable with the CUTLASS scan period.

One point must be stressed regarding the comparison of EISCAT and CUTLASS observations: the CUTLASS range cell at the location of EISCAT covers an area of ~2250 km^2 (45 km × 50 km) as opposed to 7 km^2 in the case of the EISCAT beam (0.6° half-power beam width projected to 250 km altitude). In addition, the EISCAT returns are integrated over 2 min, whereas CUTLASS samples the scatter volume for 7 s in each 2 min scan. Clearly, the scatter volumes and the temporal sampling schemes of the two radars are not identical, and some discrepancies between the observations are therefore to be expected.

Finally, measurements of nondeviative D region absorption of HF radio waves at 38.2 MHz are provided by the Imaging Riometer for Ionospheric Studies (IRIS) facility located at Kilpisjärvi, Finland (69.1°N, 20.8°E). The IRIS system can form 49 beams in a 7×7 array, one of which, beam 8, is incident on the D region over the location of EISCAT.

3. Observations

During the interval of interest, 1800 UT, June 18, 1996, to 0600 UT, June 19, 1996, the EISCAT radar was located between 2000 and 0800 magnetic local time (MLT) (at EISCAT, MLT ≈ UT + 2). Two Pi2 signatures were observed in midlatitude magnetograms during this period: the first at 1820 UT and the second at 2320 UT, when EISCAT was located near 2030 and 0130 MLT, respectively. The radar observations made during this interval are illustrated in Figures 1 and 2. Figures 1a-1f and 2a-2f illustrate the ionospheric parameters measured by EISCAT, while

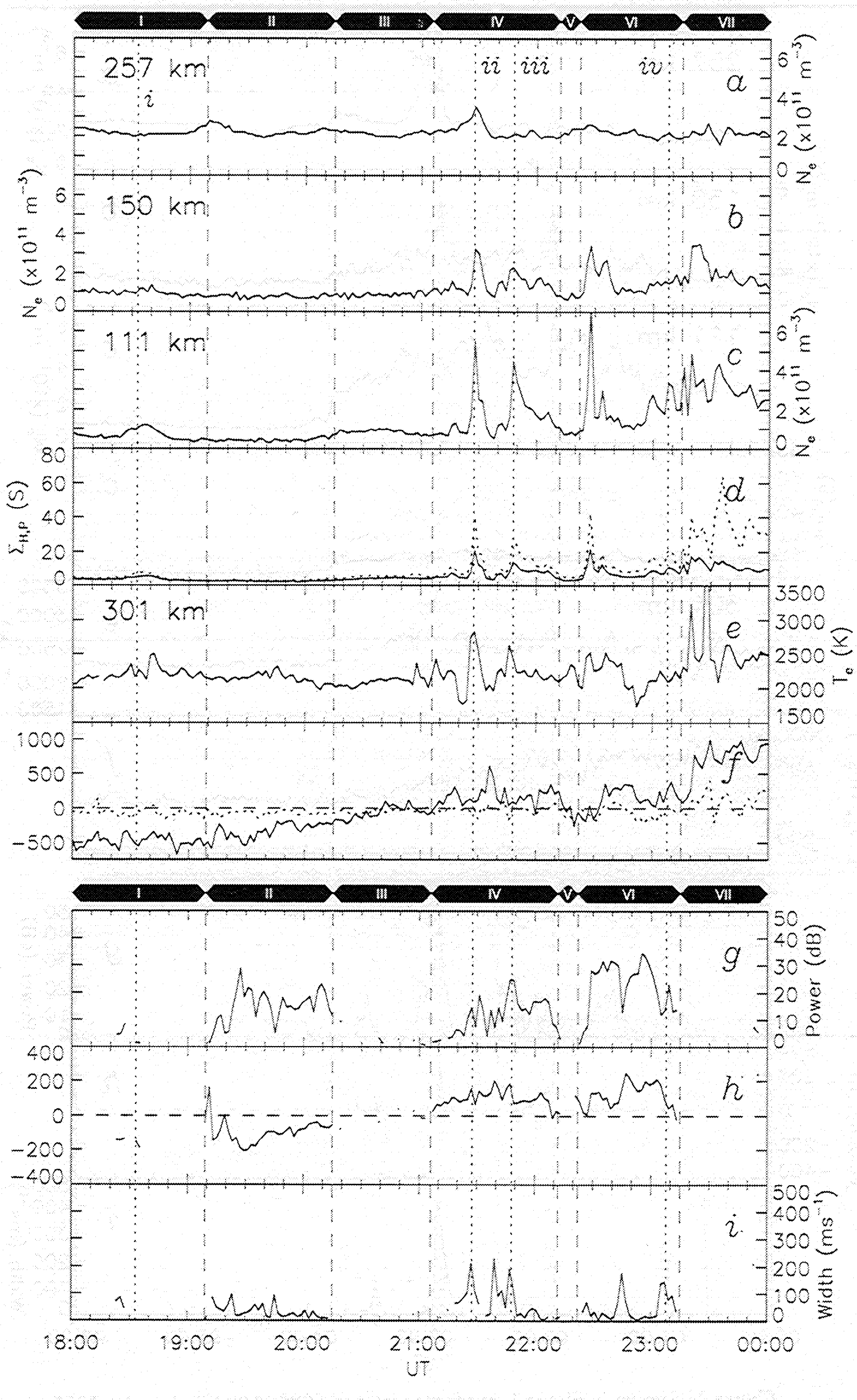

Figure 1. (a-f) Plasma parameters and electric field deduced from European Incoherent Scatter (EISCAT) radar backscatter characteristics and (g-i) Coordinated UK Twin Located Auroral Sounding System (CUTLASS) backscatter characteristics. Measurements are from the EISCAT location, beam 5, range gate 16, for the interval 1800-2400 UT, June 18, 1996. Figures 1a-1c show N_e at 257, 150, and 111 km. Figure 1d shows height-integrated Pedersen (solid curve) and Hall (dashed curve) conductivity. Figure 1e shows T_e at 301 km. Figure 1f shows v_e (solid curve) and v_n (dashed curve). Figure 1g shows backscatter power. Figure 1h shows line-of-sight Doppler velocity. Figure 1i shows spectral width.

Figures 1g-1i and 2g-2i illustrate backscatter observations of the CUTLASS Finland radar. The EISCAT measurements are as follows: Figures 1a-1c and 2a-2c are electron density N_e from three representative altitudes, 257 km (near the peak of the F region), 150 km, and 111 km (near the peak of the E region); Figures 1d and 2d are the Hall and Pedersen conductances (height-integrated conductivities), Σ_H and Σ_P; Figures 1e and 2e illustrate the electron temperature T_e at an altitude of 301 km; and Figures 1f and

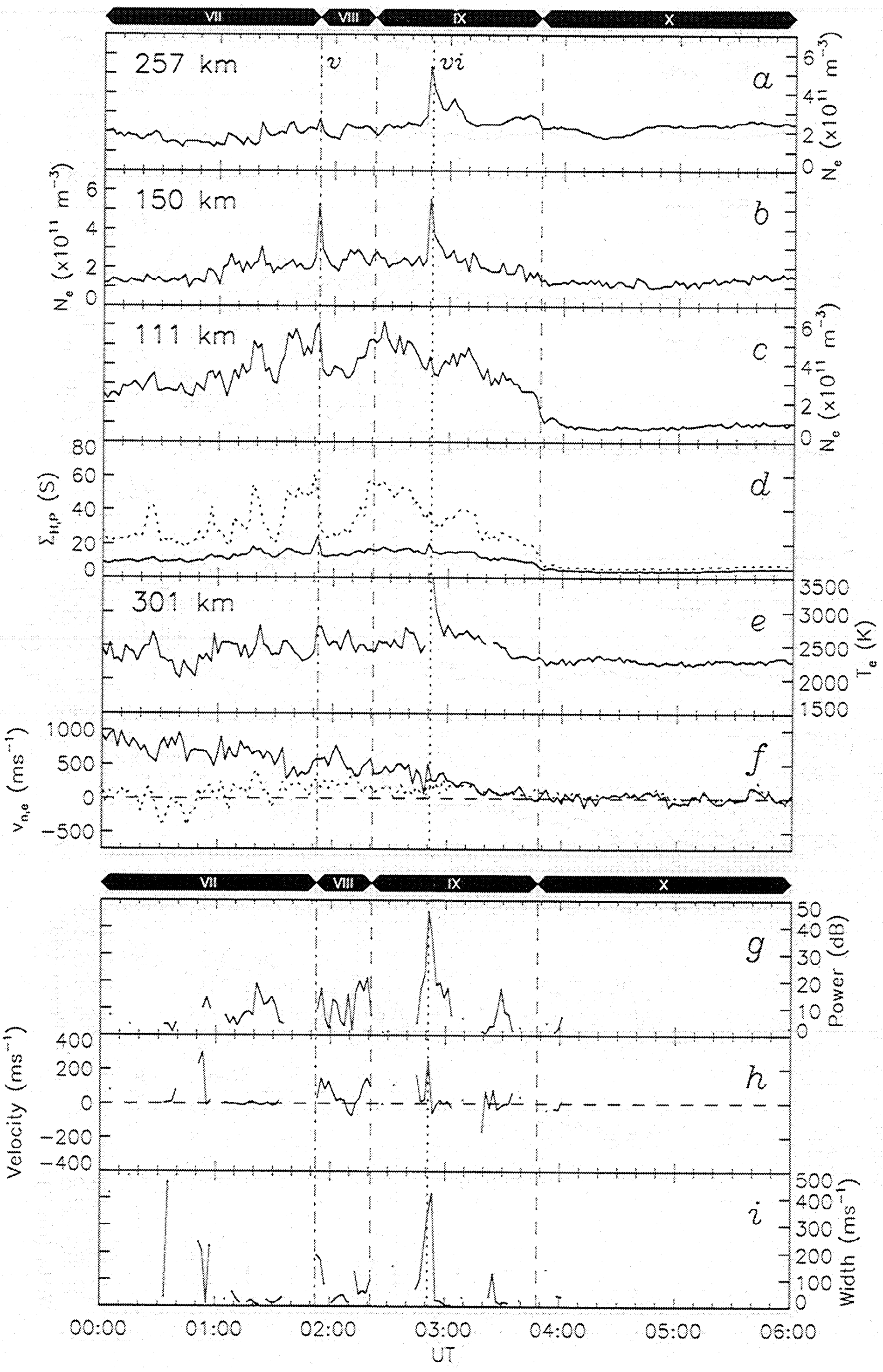

Figure 2. Similar to Figure 1, but for the interval 0000-0600 UT, June 19, 1996.

2f illustrate the geomagnetic northward and eastward components of the ion drift, v_n and v_e, measured at the tristatic intersection altitude. Note that v_n is small at all times and that in general the total velocity magnitude $v_{\mathrm{mag}} \approx |v_e|$; in other words, the flow is generally zonal with only a very small meridional component. The CUTLASS observations illustrated in Figures 1g-1i and 2g-2i are the backscatter power, the line-of-sight Doppler velocity (line-of-sight irregularity drift velocity) v_{los}, and the spectral width Δv, respectively, measured in gate 16 of beam 5, colocated with the EISCAT observations. To place these observations in some context, Plate 1 illustrates range-time-parameter plots of power, velocity, and elevation angle, along a portion of beam 5 of the CUTLASS radar, covering the geomagnetic latitude range 60.0°-83.5°N. In common with Figures 1h and 2h, positive (negative) velocities indicate motion toward (away from) the radar. Grey regions indicate backscatter which has been interpreted as ground backscatter by virtue of it having low velocity, $|v_{\mathrm{los}}| < 50$ m s^{-1}, and low spectral width, $\Delta v < 20$ m s^{-1}; in general, ground back-

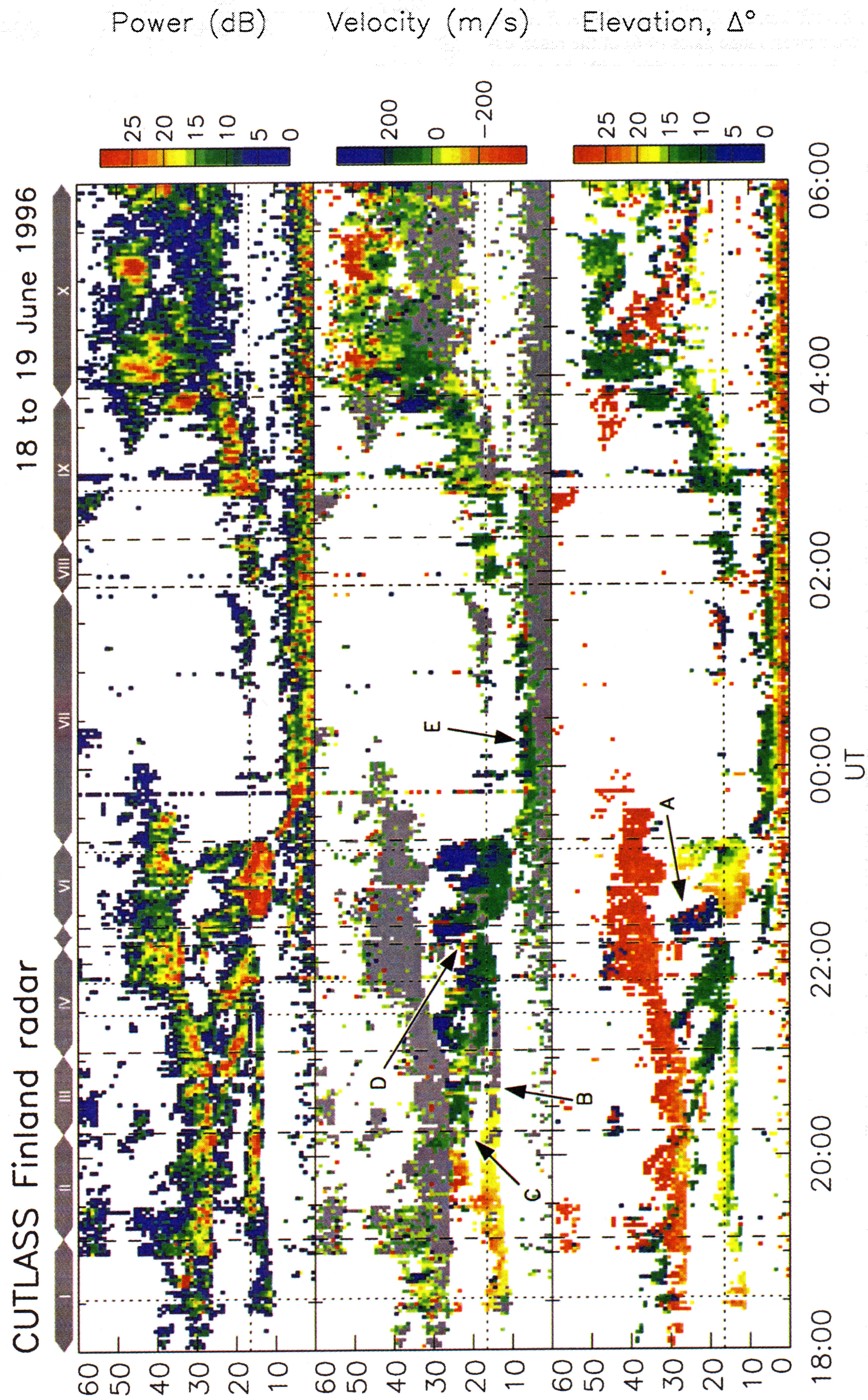

Plate 1. Range-time-parameter plots from beam 5 of the CUTLASS Finland radar between 1800 UT, June 18, 1996, and 0600 UT, June 19, 1996. The three plots correspond to backscatter power, line-of-sight Doppler velocity, and elevation angle of backscatter arrival. Gate 16, the location of the EISCAT radar is indicated by horizontal dotted lines.

scatter is of little interest to this study. In addition to true coherent ionospheric backscatter, meteor scatter, radar backscatter from the ionization trails of meteoroids [*Hall et al.*, 1997], occurs in the altitude range 80-100 km, the *D* region and lower *E* region. This is observed in the nearest range gates (0-6) of the radar, especially after 2000 UT. As meteor trails drift with the neutral wind velocity, which tends to be low at these altitudes, the ACF analysis technique has misidentified most of this scatter as ground backscatter.

To aid the discussion below, vertical lines have been superimposed on Figures 1 and 2 and Plate 1, indicating times and intervals of note. Dashed lines indicate the beginning and end of intervals of time (numbered I-X), and dotted lines indicate times when short-lived features appear simultaneously in both the EISCAT and CUTLASS observations (numbered i-vi).

First, the EISCAT observations will be briefly described. At 1800 UT the ion drift velocity is directed westward with a magnitude of approximately 500 m s^{-1}. Thereafter, the ion velocity decreases to 0 m s^{-1} near 2150 UT (during interval III) and then increases in an eastward direction; though the velocity reduces to near 0 m s^{-1} again near 2220 UT, by 0000 UT it has peaked at an eastward velocity of 1000 m s^{-1}, a sharp increase being observed at approximately 2320 UT. Over the next few hours the velocity once more decreases, reaching 0 m s^{-1} by approximately 0350 UT. This velocity signature is fairly typical of EISCAT measurements [*Davies and Lester*, 1999] and relates to the observation first of the eastward electrojet in the premidnight sector and then of the westward electrojet in the postmidnight sector. At earlier and later times the electrojets are located poleward of the EISCAT viewing area. The sharp increase in velocity observed at 2320 UT corresponds to the onset of the expansion phase of a substorm, as indicated by the second midlatitude Pi2 signature, mentioned above. Few features are observed in the electron density and conductance (3 S) measurements prior to 2015 UT. A typical N_e profile from this interval (2000 UT) is illustrated in Figure 3a: the *F* region electron density peaks at 2.1×10^{11} m^{-3}, and there is no clear *E* region ledge. There is, however, a factor of 2 increase in the *E* region electron density between 1820 and 1850 UT, which follows the first Pi2 signature, and a small increase in the *F* region electron density, to 2.9×10^{11} m^{-3}, between 1900 and 1920 UT. Between 2015 and 2110 UT, the *E* region electron density and the conductances increase by a factor of almost 2 as illustrated in Figure 3b (2040 UT). Thereafter, between 2110 and 0350 UT, the conductances and the electron densities (especially in the lower ionosphere) increase dramatically and become highly structured. Short-lived but intense increases in the conductances (over 20 S) and electron densities (over 4×10^{11} m^{-3}), especially at 2128, 2148, 2228, 2322, 0152, and 0250 UT, correspond to the passage of auroral arcs through the EISCAT beam; Figure 3c (2128 UT) illustrates the electron density profile during such an arc. That these enhanced electron densities are associated with precipitation can be demonstrated by their general correspondence with enhancements of the *F* region electron temperature [*Schunk and Nagy*, 1978]. After the onset of the substorm (intervals VII to IX) the Pedersen and Hall conductances and *E* region electron density remain consistently high, between 10 and 20 S, between 20 and 60 S, and above 3×10^{11} m^{-3}, respectively. Figures 3d (0032 UT), 3e (0136 UT), and 3f (0152 UT) illustrate N_e profiles from this period when the Hall conductance is high (20 S), very high (50 S), and very high with electron densities enhanced at all altitudes (40 S), respectively. After 0350 UT the electron densities and conductances return to their original low levels.

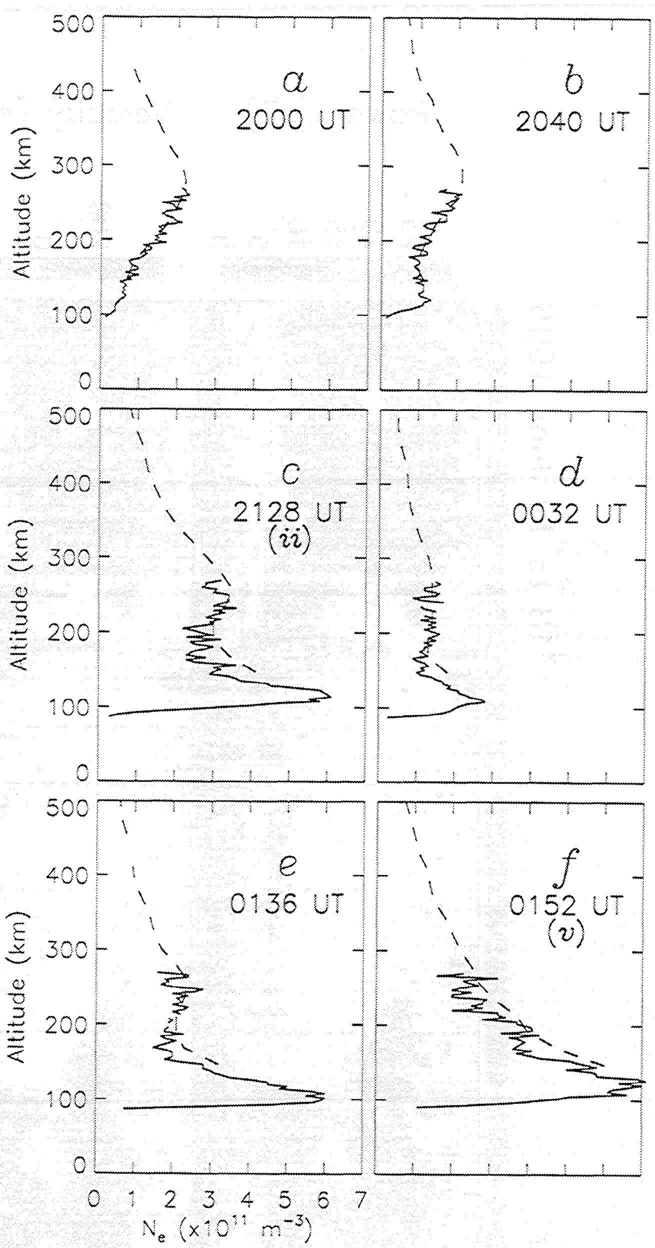

Figure 3. Vertical profiles of electron density determined by EISCAT at (a) 2000 UT, (b) 2040 UT, (c) 2128 UT, (d) 0032 UT, (e) 0136 UT, and (f) 0152 UT. The solid and dashed curves denote the alternating code and long-pulse measurements, respectively.

Whilst EISCAT measurements are available throughout the interval of study, CUTLASS backscatter only appears at the location of EISCAT during the intervals II, IV, VI, and VIII (with a few exceptions which will be discussed below). During interval II, when EISCAT measured westward ion drift, the CUTLASS line-of-sight irregularity drift velocity was negative (away from the radar). As beam 5 points some 29° west of geomagnetic north at the latitude of EISCAT, $v_{los} < 0$ m s^{-1} is consistent with westward flow. Similarly, during intervals IV and VI, $v_{los} > 0$ m s^{-1}, consistent with the eastward ion drift observed by EISCAT. Indeed, it was demonstrated by *Davies et al.* [1999] for intervals II, IV, and VI that when the EISCAT tristatic measurement of ion drift was resolved along the CUTLASS beam, excellent agreement was found with v_{los}. This agreement is illustrated in Figure

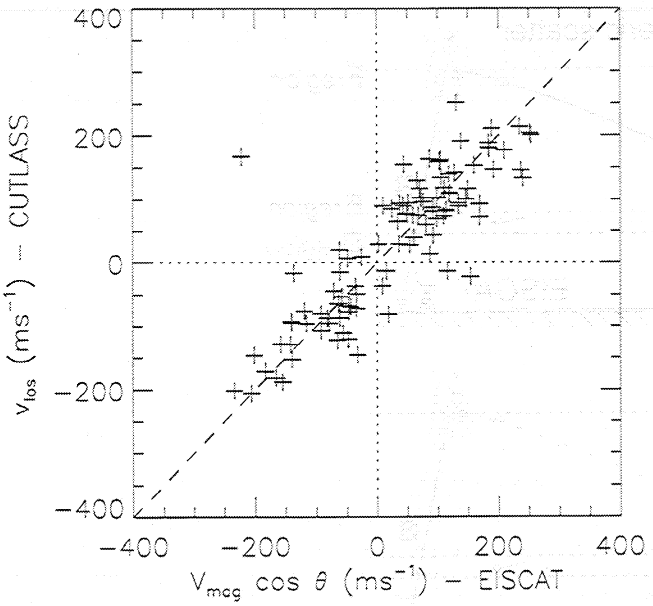

Figure 4. A comparison of the Doppler velocity measured by the CUTLASS radar at the EISCAT location and the EISCAT tristatic measurements of the bulk ion drift, resolved along the CUTLASS beam direction.

4, in which v_{los} is plotted as a function of $v_{mag}\cos\theta$, where θ is the angle between the flow direction determined by EISCAT and the CUTLASS beam; a coefficient of correlation of 0.68 is found.

The coherent backscatter power tends to vary between 0 and 30 dB during the interval of study, without any obvious trend (Figures 1g and 2g). In part, these variations will be due to HF propagation effects, such as focusing and defocusing, and changes in the elevation angle, on which the gain of the CUTLASS antennas is dependent. However, there are occasions when local peaks in the backscatter power are found to correspond to the passage of auroral arcs through the EISCAT beam, specifically at 2128, 2148, 2308, and 0252 UT (times marked ii, iii, iv and vi). Similarly, in the case of spectral width, which most often takes values below 100 m s^{-1}, local enhancements to 200 m s^{-1} and more are found to correspond to auroral arcs at 2128, 2148, 2308, 0152, and 0252 UT (times marked ii, iii, iv, v and vi).

Plate 1 allows the observations to be placed in context. Backscatter first appears near the latitude of EISCAT at 1820 UT, at the time of the first Pi2 signature and the brief enhancement of the *E* region electron density observed by EISCAT. This region of backscatter is only a few range gates, approximately 250 km, in latitudinal extent and has an elevation angle of $\Delta \approx 22^\circ$. After 1900 UT, during interval II, a new region of backscatter with $\Delta \approx 16^\circ$ appears at EISCAT but progresses equatorward of EISCAT during intervals III and IV. Meanwhile, from 1930 at 2220 UT, another region of ionospheric backscatter appears poleward of EISCAT (near range gate 25) and progresses equatorward, crossing the latitude of EISCAT during interval IV; this region of backscatter has $\Delta \approx 12^\circ$. During interval V no backscatter is present at the latitude of EISCAT; though poleward of this, a region of backscatter is observed, with $\Delta \approx 0^\circ$-5° (marked A in Plate 1). A new region of backscatter, with $\Delta \approx 15^\circ$-22°, appears at EISCAT during interval VI. Only sporadic backscatter is observed at the EISCAT location thereafter, except during interval VIII. During interval X the electrojet-associated backscatter is observed to have progressed to higher latitudes, away from the EISCAT location. The elevation angle measurements indicate that there is significant variability in the altitude at which the backscatter originates throughout the interval. At the range of EISCAT, elevation angles of $\Delta = 0^\circ$-5°, 10°, and 20° correspond to altitudes of 120, 220, and 360 km, assuming little ionospheric refraction. Hence all backscatter observed over EISCAT during this interval originates in the *F* region, though intervals of *E* region scatter are observed at other latitudes (A in Plate 1).

4. Discussion

Two substorms, indicated by midlatitude Pi2s, occur during the interval of study, and the behavior of the CUTLASS Finland radar backscatter is different during each. Following the first substorm (1820 UT, time i), when the radars are located in the premidnight sector, a region of backscatter appears near the location of EISCAT; this is despite severe HF interference at this time. Following the second substorm, when the radars are located near 0000 MLT, there is a large, prolonged reduction in the amount of ionospheric backscatter observed, especially at the latitude of EISCAT. Clearly, different geophysical processes occur in different MLT sectors during substorm onset. Unfortunately, because of the interference suffered by the radar prior to 1900 UT, the first event cannot be investigated in detail. For the rest of the interval of study, however, the conditions under which backscatter is observed by coherent HF radars and the factors that influence the backscatter intensity and spectral width will be discussed in turn in sections 4.1-4.3.

4.1. Backscatter Dropout During Intervals of Low Electric Field

There are three intervals (III, V, and X) when backscatter is absent at the latitude of EISCAT, coincident with small tristatic ion drift velocities, approximately less than 100 m s^{-1}, equivalent to an electric field of 5 mV m^{-1} or less. This suggests that in the absence of other energy sources, the growth of *F* region irregularities is dependent on the presence of an applied electric field, consistent with the description of the **E×B** instability given in section 1, where the growth rate was shown to be proportional to E or $E^{1/2}$. This does not necessarily preclude the observation of coherent scatter with near-zero line-of-sight velocities, indicative of a near-zero electric field component perpendicular to the radar beam ($E_\perp = v_{los}/B$). However, in such a situation, it is proposed, there would have to be a significant electric field component parallel to the radar beam and hence plasma drift perpendicular to the beam. Indeed, such near-zero v_{los} is observed during intervals III and IV, at latitudes just equatorward of EISCAT (marked B in Plate 1), which has been misidentified as ground backscatter owing to its low velocity and low spectral width.

Extrapolating from these observations, the presence of a region of near-zero electric field within the electrojet can be postulated from the absence of backscatter in a channel progressing from range gate 20 at 1930 UT to range gate 15 at 2120 UT (marked C in Plate 1). A similar $E \approx 0$ mV m^{-1} region is observed to progress from range gate 25 at 2212 UT to range gate 15 at 2322 UT (marked D). The measured electric field is again near-zero after 0350 UT, during interval X; the CUTLASS backscatter indicates that the electrojet has progressed poleward of EISCAT at this time. Such a relationship between radar aurora and electrojet activity has previously been found for VHF radars observing in the auroral *E* region [see *Greenwald et al.*, 1975, and references therein].

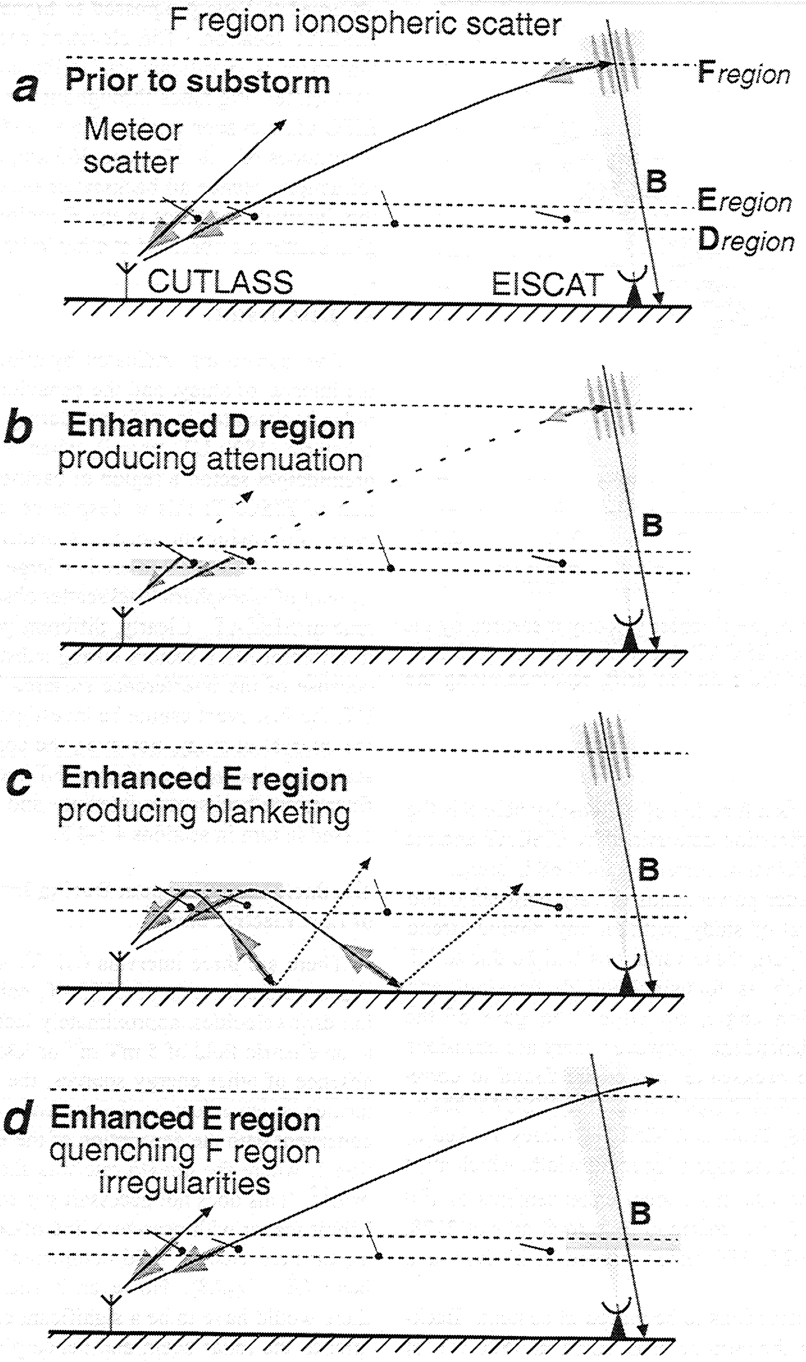

Figure 5. Four schematic diagrams illustrating possible mechanisms for the dropout in backscatter following substorm breakup (see text for details): (a) the situation prior to substorm onset when *F* region backscatter is observed, (b) enhanced *D* region electron density producing attenuation of the radar signal, (c) enhanced *E* region backscatter producing blanketing of the *F* region, and (d) enhanced *E* region electron density, conjugate to the *F* region irregularities, producing a decay in the irregularity growth rate.

It should be noted that the growth rate of irregularities is dependent not only on *E* but also on L^{-1}, where, in general, *L* is the scale length of the electron density gradient perpendicular to **B**: the growth rate is enhanced in the presence of steep gradients; conversely, in the absence of gradients no irregularities are generated. Hence it is possible to have regions of high electric field but in which no scatter would be observed. Unfortunately, the EISCAT observations only allow an estimate of N_e to be made and not ∇N_e (at least not in the horizontal direction). The role of electron density gradients will be discussed further in section 4.3.

4.2. Backscatter Dropout in the Midnight Sector Following Substorm Onset

Following the second Pi2 pulsation, indicative of the onset of the second substorm, between 2315 and 0350 UT (intervals VII and IX) there is a significant dropout in the amount of backscatter

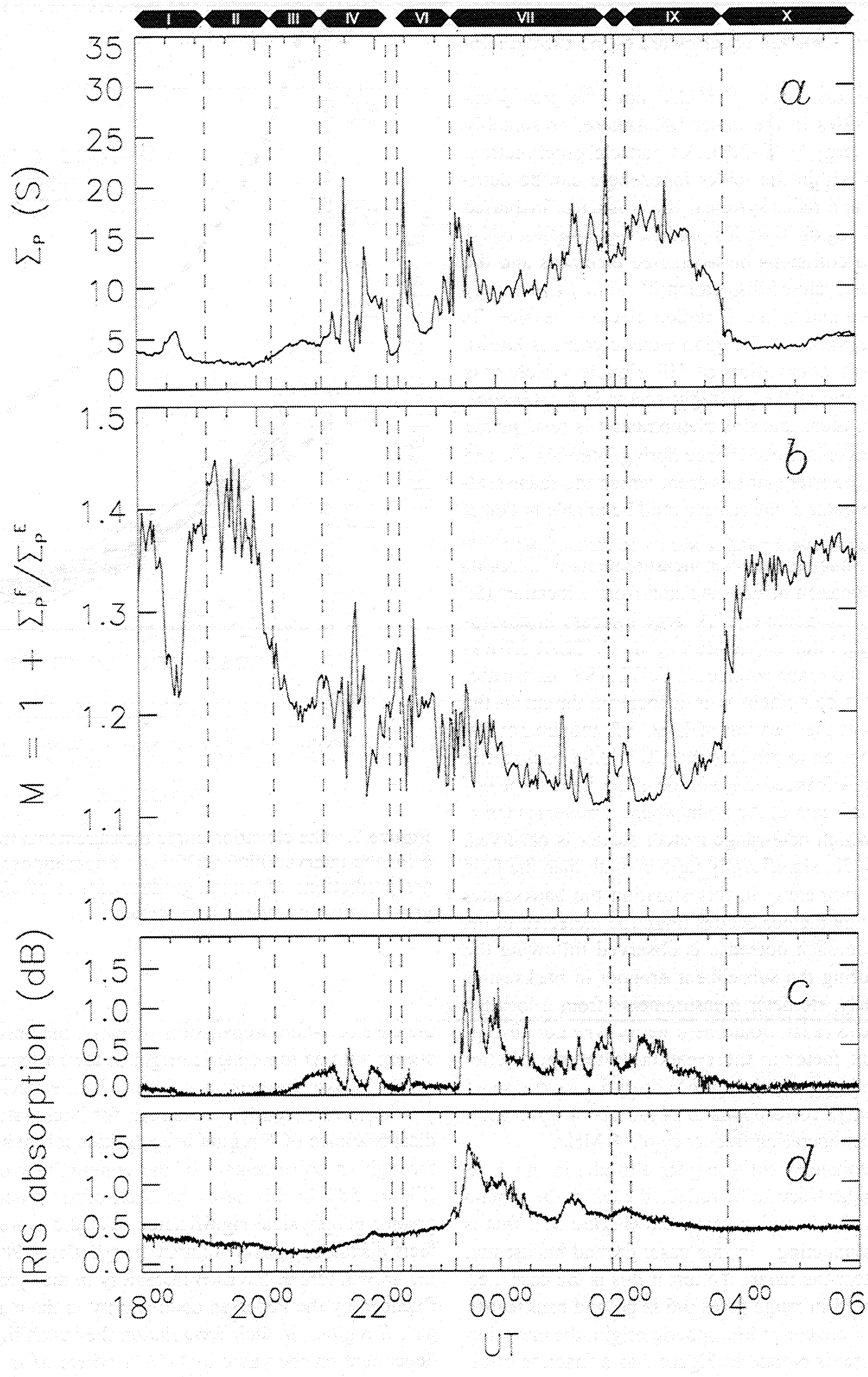

Figure 6. (a) The total height-integrated Pedersen conductivity determined by EISCAT, for the interval 1800 UT, June 18, 1996, to 0600 UT, June 19, 1996. (b) A determination of M, a measure of the ratio of the Pedersen conductivity in the E and F regions. (c, d) Imaging Riometer for Ionospheric Studies (IRIS) measurements of D region absorption from the location of EISCAT and 150 km south of EISCAT, respectively.

observed by the CUTLASS Finland radar at the location of EISCAT, though ionospheric backscatter is then observed at lower latitudes, equatorward of range gate 10 (marked E in Plate 1), indicating the equatorward expansion of the substorm electrojet system. There are several candidate mechanisms for the backscatter dropout, and these will be discussed below, with reference to the schematic diagrams in Figure 5. Figure 5a illustrates the situation prior to substorm onset, with the predominant region of backscatter originating near the location of EISCAT, scattered from field-aligned electron density perturbations in the F region. In addition to this is meteor scatter originating in the D region and lower E region. This is observed predominantly in the nearest range gates and indicates the point at which the radar beam traverses the *D* region, ~500 km equatorward of the EISCAT location.

Subsequent to substorm onset, EISCAT measures greatly enhanced electron densities in the lower ionosphere, presumably produced by high-energy (~10-30 keV) particle precipitation. Enhanced ionization within the lower ionosphere can be detrimental for HF radio and radar systems. For instance, increased electron density at *D* region altitudes produces attenuation of HF radio signals through collisions between free electrons and the neutral atmosphere, the rate of dissipation of radio wave energy being directly proportional to the *D* region electron density. In particular, substorm-associated *D* region enhancement is known to produce significant attenuation of HF signals which pass through the auroral zone in the midnight sector [e.g., *Akasofu*, 1968]. It is possible, then, that this phenomenon is responsible for the dropout in backscatter occurrence during intervals VII and IX. In other words, the irregularities from which the radar scatters could still be present, but the radar would be unable to detect them owing to absorption of the probing radio wave. Figures 6c and 6d present IRIS imaging riometer measurements of *D* region absorption from the location of EISCAT and from a location 150 km south of EISCAT, respectively. A large increase in absorption is observed during interval VII, during the CUTLASS backscatter dropout, and the reappearance of CUTLASS backscatter during interval VIII is coincident with a local minimum in the measured absorption at the location of EISCAT, though not farther south. For absorption to produce the CUTLASS backscatter dropout, however, the enhanced electron densities have to be coincident with the radar beam at the point where it traverses the *D* region, the point at which near-range meteor scatter is observed, as indicated in Figure 5b, significantly farther south than the field of view of the IRIS riometer. In this situation the backscatter power of the near-range meteor echoes might be expected to decrease also, though no such decrease is observed following the substorm onset or during the subsequent dropout in backscatter over EISCAT. Clearly, riometer measurements from a location closer to the CUTLASS radar would help verify whether absorption was a significant factor in the creation of the backscatter dropout. It should be noted that 1.5 dB of absorption as measured by a riometer at 40 MHz corresponds to 70-90 dB of absorption of the radar signal at an operating frequency of 10 MHz.

Electron density enhancement at higher altitude, in the *E* region, can cause the radar beam to be reflected back to the ground and hence not reach the *F* region scatterers (Figure 5c); this is known as *E* region blanketing. In this case, ground backscatter should be observed near the radar. To test if this is the case, i.e., the backscatter observed in range gates 0-6 is ground backscatter as opposed to being of meteor or ionospheric origin, the elevation angle of this backscatter is plotted in Figure 7 as a function of radar range, for each scan between 0000 and 0020 UT. The elevation angle decreases with increasing range, as expected for scatter originating in, or reflected from, an ionospheric layer of uniform altitude. Superimposed on Figure 7 are two simple predictions of the range dependence of elevation angle: on the one hand assuming backscatter from within an ionospheric layer at an altitude of 100 km, known as 1/2-hop propagation [see *Milan et al.*, 1997b], and on the other hand assuming the reflection of ground backscatter in such a layer, known as 1-hop. The height of reflection or scatter, h, is related to the elevation angle and radar range r by $h = (R_E^2 + 2R_E r_0 \sin\Delta + r_0)^{1/2} - R_E$, where R_E is the radius of the Earth and $r_0 = r$ in the case of 1/2-hop propagation and $r_0 = r/2$ in the case of 1-hop propagation. Clearly, the observations are consistent with an ionospheric origin of the backscatter, and hence *E* region blanketing does not appear to be the mechanism in action.

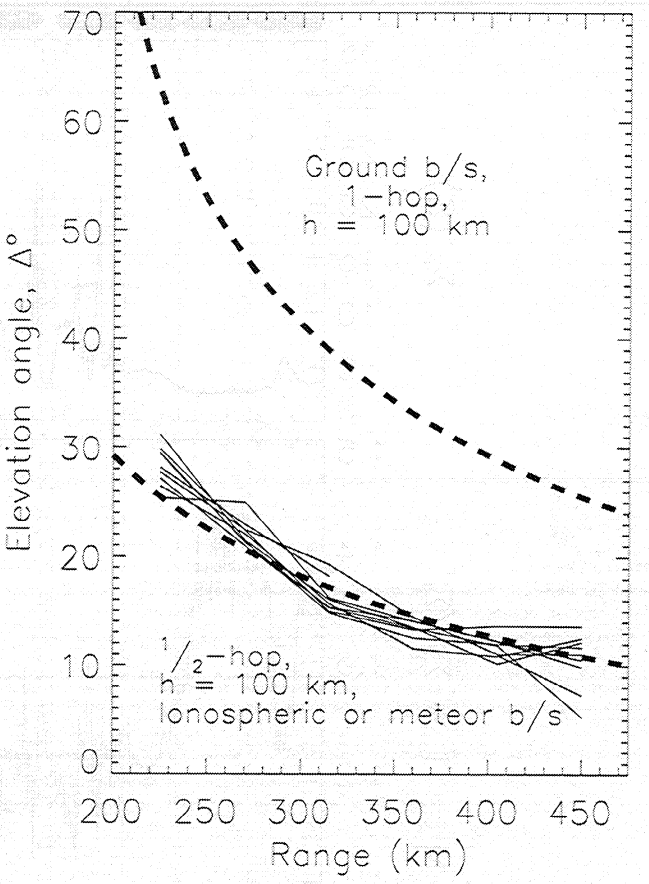

Figure 7. The elevation angle measurements from range gates 1-6 for the interval 0000-0020 UT. Superimposed (dashed curves) are predictions of the range dependence of elevation angle for ground and ionospheric backscatter.

The third possible mechanism for backscatter dropout is the disappearance of *F* region irregularities following substorm onset through an enhancement of the conductivity of the ionosphere (Figure 5d); in this case, the backscatter dropout is perhaps of greater geophysical significance than the more instrumental effects discussed above. *Vickrey and Kelley* [1982] suggested that the growth rate of the **E**×**B** instability in the *F* region could be influenced by the Pedersen conductivity in the magnetically conjugate *E* region. In their formulation the instability growth rate γ is dependent on the value of $1-M^{-1}$, where M is a measure of the relative contributions of the *F* and *E* regions to the total conductance, $M = 1 + \Sigma_{P\text{-}F}/\Sigma_{P\text{-}E}$. An examination of the altitude profile of the Pedersen conductivity indicates that the major contribution to the conductance is from the *E* region, with the *F* region contributing only ~10% of the total value. A high relative *E* region conductance, and hence low M, shorts out the perturbation electric field associated with the *F* region irregularities, the growth rate of the **E**×**B** instability becomes small, and the irregularities decay. *Tsunoda* [1988] concluded that because of high auroral *E* region electron densities, produced by auroral precipitation, very low M values of between 1 and 1.2 were expected and that as a consequence, the **E**×**B** instability may be less dominant in the auroral zone than at other latitudes. In the present case, Figure 6 illustrates both the total Pedersen conductance Σ_P determined from the EISCAT observations for the interval of interest (Figure 6a) and M (Figure 6b). It was assumed that the E region contribution to M occurred over an altitude range of 70-140 km and that the F region contribution to M occurred from altitudes above 140 km. In general, M is found to take values between 1.1 and 1.5. In particular, however, during intervals VII and IX, when little backscatter was observed by the CUTLASS radar, M is a minimum, varying between 1.1 and 1.2, consistent with the calculations of Tsunoda for precipitation events in the auroral zone. Interval VIII, a short period when backscatter was observed between intervals VII and IX, corresponds to a slight recovery of M to higher values (the backscatter observed between 0100 and 0150 UT is ground scatter and will not be considered further). Also, the appearance of backscatter at 0250 UT (time vi), the passage of an auroral arc through the EISCAT beam, also corresponds to a brief enhancement of M. Clearly, the M value is an oversimplification of the complex geophysical processes controlling the generation of irregularities. For instance, the E and F regions were chosen, somewhat arbitrarily, to meet at an altitude of 140 km, as this corresponds approximately to the valley in the N_e profiles measured by EISCAT (see, for example, Figures 3c-e). However, in a situation such as that in Figure 3f where there is no clear demarcation between the E and F regions, it is unclear how the M value should be calculated. A more rigorous approach is needed to properly investigate the effects of E region electron density enhancement on the generation of F region field-aligned irregularities.

Backscatter dropouts are a common feature of HF radar observations of substorms, though in most cases the dropout appears more as a bite-out in the preexisting backscatter region rather than as an almost complete disappearance of the backscatter, as observed in the present extreme example. The present observations suggest that the backscatter dropout is a consequence of auroral absorption of the radar radio wave or the quenching of the F region instability mechanism by enhanced Pedersen conductivities in the E region. In the latter case, the bite-out region maps the location of elevated E region electron density, and hence Pedersen conductivity, produced by high-energy substorm-associated precipitation; the poleward edge of the region of backscatter marked E in Plate 1 must correspond to the equatorward edge of the high E region conductivity region. In the former case, the dropout is indicative of an enhancement of the D region at a location somewhere equatorward of the dropout region. It is clear that both mechanisms could operate simultaneously, as both require high-energy particle precipitation to produce an enhanced electron density in the lower ionosphere.

4.3. Characteristics of Backscatter From Auroral Arcs

The passage of auroral arcs through the EISCAT beam can be deduced from enhanced E region electron densities and F region electron temperatures. For example, the enhanced E region electron densities associated with the passage of auroral arcs at times ii and v are illustrated in Figures 3c and 3f. There is often a simultaneous enhancement of the Finland radar backscatter power and spectral width. Five such cases occur at times ii, iii, iv, v, and vi, though the following discussion will concentrate on the first two of these examples. To examine the radar backscatter from these two intervals in more detail, Figure 8 illustrates six backscatter spectra, three from each arc example (Figures 8a-8c and 8d-8f), from the beam and range gate that corresponds to the EISCAT location. For each interval, the three spectra are taken from the scan prior to, during, and immediately following the passage of the arc through the EISCAT beam. The shaded spectra have been normalized to the power of the middle spectrum in each case, though the dot-dashed lines indicate the spectra self-normalized to aid comparison of the spectral shapes. During both intervals the spectra indicate that the predominant Doppler velocity within the scatter volume is $v_{los} \approx 100$ m s^{-1} and that the shape of the main spectral peak remains relatively constant. Hence the bulk plasma motion does not appear to vary significantly during the passage of the arc. However, the backscatter intensity within this main peak does increase when the arc is within the range cell, by a factor of between 3 and 10. In addition, during the passage of the arc a subsidiary peak appears within the spectra (indicated by arrows in Figures 8b and 8e), in both cases shifted by ~500 m s^{-1} above or below the main peak; the backscatter power within this subsidiary peak is comparable with the power of the main peak in the preceding and following spectrum. It is this subsidiary peak which causes the ACF analysis to return a broad spectral width at times when an arc is present.

Two possible explanations can account for the appearance of the subsidiary peaks. The first is that these peaks correspond to the intense but small-scale electric field that is known to be associated with auroral arcs [e.g., *Marklund*, 1984]. It would be expected that this intense electric field could be observed by an enhancement of the ion drift velocity measured by EISCAT, though a shorter integration period would be necessary to resolve this. Unfortunately, the signal-to-noise ratio at the EISCAT remote sites was insufficient to allow the integration period of the ion drift measurements to be reduced significantly. However, the presence of the arc electric field can be deduced from short-lived ion temperature enhancements measured by the Tromsø site when integrated at 10 s (see Figure 8g); these correspond to ion frictional heating [see *Davies et al.*, 1997, and references therein] in the presence of the intense electric field. The second explanation is that of *Villain et al.* [1987, 1990], who suggested that intense electron precipitation could produce ion acoustic and electrostatic ion cyclotron waves in the E region and lower F region, even in the presence of subcritical horizontal electron drift, from which the HF radars could scatter. Such waves would be expected to have phase speeds of the order of the local ion acoustic speed, 400-600 m s^{-1}, consistent with the present observations.

It is unclear exactly why the backscatter intensity of the main spectral peak is enhanced at these times. It is possibly due to an increase in the backscatter cross section owing to increased background electron density (the backscatter cross section of E region irregularities is proportional to N_e^2 [e.g., *Starkov et al.*, 1983]) or an increase in the irregularity growth rate associated with the steep electron density gradients produced by the structured arc precipitation. Also, potentially, the backscatter intensity may increase through an enhanced growth rate of the current convective instability in the presence of auroral arcs [*Tsunoda*, 1988].

The increase in spectral width and backscatter power in the presence of auroral arcs makes possible the mapping of the location of such features within HF radar spatial scans. Figure 9 illustrates the backscatter power measurements from the eight radar scans between 2144 and 2200 UT; the location of EISCAT is indicated by an arrow for each scan. The third scan corresponds to the passage of the auroral arc over EISCAT at time iii. In the first scan a northeast-southwest aligned feature is observed just poleward of the EISCAT location. In the second scan a similar fea-

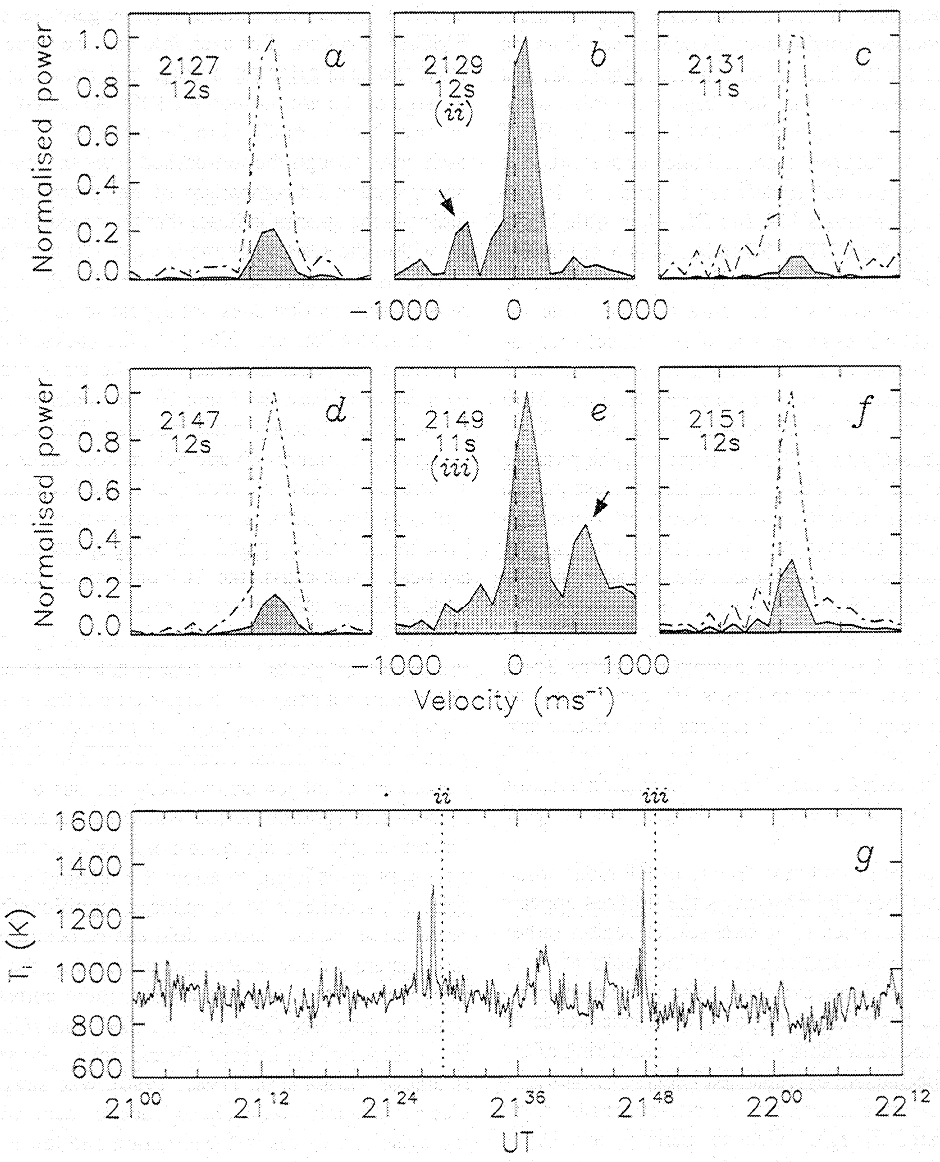

Figure 8. (a-f) Six backscatter spectra observed by the CUTLASS radar at the location of EISCAT taken from times near the passage of two auroral arcs through the EISCAT beam and (g) 10 s integration ion temperature as measured by EISCAT at an altitude of 301 km. The vertical dotted lines in Figure 8g indicate the times of the CUTLASS soundings corresponding to Figures 8b and 8e.

ture appears just to the south of EISCAT, and in the subsequent scans these two features drift eastward and out of the field of view of the radar. During the third scan the southwest end of the first feature crosses the location of EISCAT, and the auroral arc is observed in the incoherent radar measurements. In addition, other enhanced backscatter power features appear within the CUTLASS field of view during this interval: for instance a feature forms to the northwest of the EISCAT location in the second scan, which by the end of the interval has extended east-west across most of the field of view. It is clear that backscatter power can be related to geophysical features which, especially with the higher temporal and spatial resolutions that can be achieved by the SuperDARN radars, can be traced over large regions of the polar ionosphere with the HF radar technique.

5. Conclusions

The spectral characteristics of coherent backscatter from decameter-wavelength ionospheric *F* region field-aligned irregularities have been compared with common volume plasma parameters and tristatic measurements of the bulk ion drift velocity deduced by incoherent scatter techniques. The main conclusions of the study are as follows.

1. In the absence of other energy sources, backscatter is present only when the convection electric field is nonzero (in the absence of significant neutral winds), because the growth rate of the **E**×**B** instability is dependent on the velocity of the bulk ion drift relative to the neutral background. If the neutral wind velocity increases to equal the bulk ion drift, the growth rate of the insta-

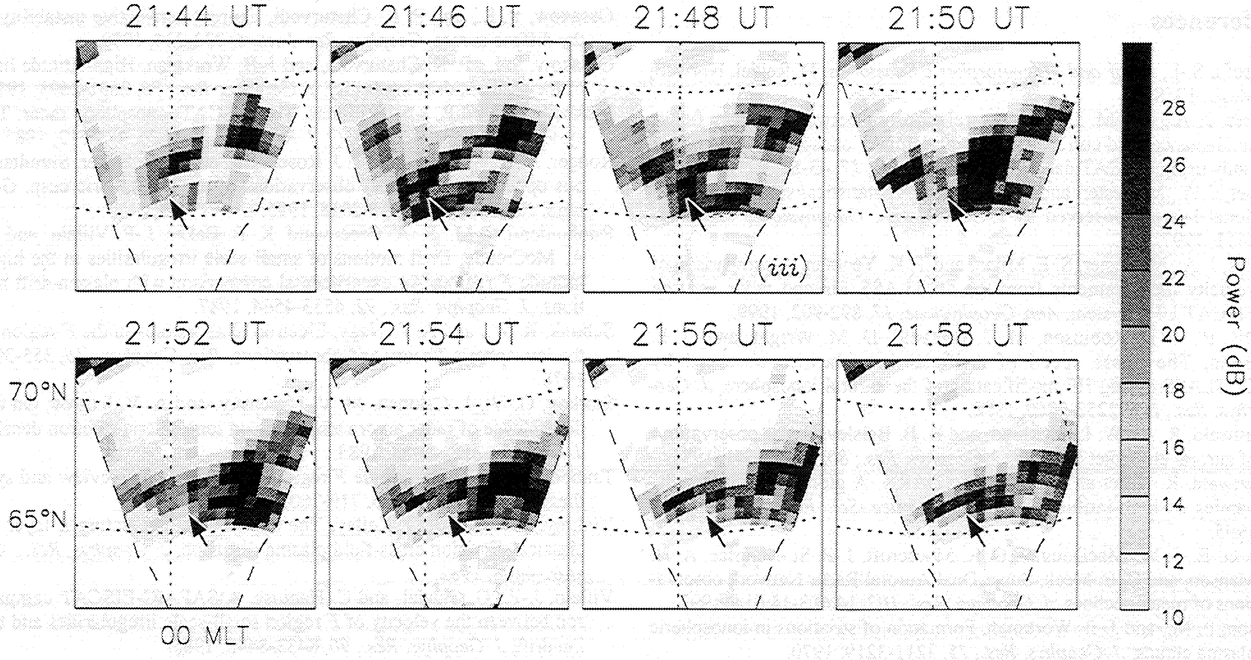

Figure 9. Backscatter intensity measured in eight sequential CUTLASS scans, between 2144 and 2200 UT, June 18, 1996. The arrows indicate the location of EISCAT.

bility would become low, but such a situation generally arises only after several hours of constant applied electric field, as the response time of the neutral atmosphere to ion drag is slow. The irregularity growth rate is also dependent on the scale length of the background electron density gradient in the ionosphere also, but we have not been able to determine this in the present study.

2. During periods of ionospheric electron density enhancement by auroral precipitation, HF radar backscatter can suffer from dropouts or bite-outs. Two possible mechanisms for the loss of backscatter have been identified. In the first, enhanced *D* region electron densities produce attenuation of the radar radio wave, known as auroral absorption. In the second, an enhanced *E* region electron density can result in high Pedersen conductivity, which acts to short-out the perturbation electric field associated with *F* region irregularities and causes them to decay.

3. The intense but short-lived (within the volume of observations) electron precipitation associated with auroral arcs can (1) give rise to backscatter, where backscatter is not already present or (2) produce an enhancement of the backscatter intensity of a region of preexisting backscatter. This enhancement is possibly associated with an increase in the growth rate of the current convective instability in the presence of the arc or an increase in the growth rate of the **E**×**B** instability due to a steepening of electron density gradients. Moreover, the auroral arc produces a subsidiary peak in backscatter spectra, resulting in a broadening of the spectral width attributed to the backscatter. The subsidiary peak is thought to be a consequence of the high electric field associated with the arc electrodynamics. Both increased backscatter power and spectral width should make possible the mapping of auroral arcs and other precipitation features with the HF radar technique.

4. The elevation angle from which backscatter returns are observed at the location of EISCAT varies throughout the interval of study. However, at all times during the present interval all backscatter originates at *F* region altitudes, though there are occasions when *E* region scatter is observed away from the location of EISCAT (for instance, the location marked A in Plate 1). This indicates that, as discussed by *Milan et al.* [1998], the HF radar technique is often capable of exploiting irregularities at whichever altitude they occur to provide backscatter.

5. Clearly, the HF coherent radar and UHF incoherent radar techniques are complementary. The coherent radar allows the point measurements of the incoherent radar to be placed within the context of the large-scale convection pattern, whereas the incoherent radar gives detailed information about the physical processes occurring at a point within the coherent radar field of view. The overall CUTLASS system comprises two radars: the Finland radar and a radar located on Iceland. These two coherent radars have two incoherent radars within their common observing volume: the EISCAT facility employed in the present study and the EISCAT Svalbard radar (ESR) located within the polar cap at Longyearbyen on Svalbard. More extensive studies involving all four radars will help answer many outstanding questions about the magnetosphere-ionosphere system.

Acknowledgments. CUTLASS is supported by the Particle Physics and Astronomy Research Council (PPARC grant PPA/R/R/1997/00256), United Kingdom, the Swedish Institute for Space Physics, Uppsala, and the Finnish Meteorological Institute, Helsinki. EISCAT is an international facility funded collaboratively by the research councils of Finland (SA), France (CNRS), the Federal Republic of Germany (MPG), Japan (NIPR), Norway (NAVF), Sweden (NFR), and the United Kingdom (PPARC). The authors are indebted to the director and staff of EISCAT for operating the facility and supplying the data and to the EISCAT group at the Rutherford Appleton Laboratory for additional assistance. The IRIS riometer is operated by the Communications Research Centre at Lancaster University (UK) and is funded by PPARC in collaboration with the Sodankylä Geophysical Observatory. SEM and JAD are supported on PPARC grant PPA/G/O/1997/000254.

Michel Blanc thanks Jean-Paul Villain and Raymond A. Greenwald for their assistance in evaluating this paper.

References

Akasofu, S.-I., *Polar and Magnetospheric Substorms*, D. Reidel, Norwell, Mass., 1968.

Davies, J. A., and M. Lester, The relationship between electric fields, conductances and currents in the high-latitude ionosphere: A statistical study using EISCAT data, *Ann. Geophysicae*, *17*, 43-52, 1999.

Davies, J. A., M. Lester, and I. W. McCrea, A statistical study of ion frictional heating observed by EISCAT, *Ann. Geophysicae*, *15*, 1399-1411, 1997.

Davies, J. A., M. Lester, S. E. Milan, and T. K. Yeoman, A comparison of velocity measurements from the CUTLASS Finland radar and the EISCAT UHF system, *Ann. Geophysicae*, *17*, 892-902, 1999.

Eglitis, P., T. R. Robinson, M. T. Rietveld, D. M. Wright, and G. E. Bond, The phase speed of artificial irregularities observed by CUTLASS during HF modification of the auroral ionosphere, *J. Geophys. Res.*, *103*, 2253-2260, 1998.

Greenwald, R. A., W. L. Ecklund, and B. B. Balsley, Radar observations of auroral electrojet currents, *J. Geophys. Res.*, *80*, 3635-3641, 1975.

Greenwald, R. A., et al., DARN/SuperDARN: A global view of the dynamics of high-latitude convection, *Space Sci. Rev.*, *71*, 761-796, 1995.

Hall, G. E., J. W. MacDougall, D. R. Moorcroft, J.-P. St.-Maurice, A. H. Manson, and C. E. Meek, Super Dual Auroral Radar Network observations of meteor echoes, *J. Geophys. Res.*, *102*, 14,603-14,614, 1997.

Linson, L. M., and J. B. Workman, Formation of striations in ionospheric plasma clouds, *J. Geophys. Res.*, *75*, 3211-3219, 1970.

Marklund, G., Auroral arc classification scheme based on the observed arc-associated electric field pattern, *Planet. Space Sci.*, *32*, 193-211, 1984.

Milan, S. E., T. B. Jones, T. R. Robinson, E. C. Thomas, and T. K. Yeoman, Interferometric evidence for the observation of ground backscatter originating behind the CUTLASS coherent HF radars, *Ann. Geophysicae*, *15*, 29-39, 1997a.

Milan, S. E., T. K. Yeoman, M. Lester, E. C. Thomas, and T. B. Jones, Initial backscatter occurrence statistics from the CUTLASS HF radars, *Ann. Geophysicae*, *15*, 703-718, 1997b.

Milan, S. E., T. K. Yeoman, and M. Lester, The dayside auroral zone as a hard target for coherent HF radars, *Geophys. Res. Lett.*, *25*, 3717-3720, 1998.

Milan, S. E., M. Lester, S. W. H. Cowley, J. Moen, P. E. Sandholt, and C. J. Owen, Meridian-scanning photometer, coherent HF radar, and magnetometer observations of the cusp: A case study, *Ann. Geophysicae*, *17*, 159-172, 1999.

Ossakow, S. L., and P. K. Chaturvedi, Current convective instability in the diffuse aurora, *Geophys. Res. Lett.*, *6*, 332-334, 1979.

Ossakow, S. L., P. K. Chaturvedi, and J. B. Workman, High-altitude limit of the gradient drift instability, *J. Geophys. Res.*, *83*, 2691-2693, 1978.

Rishbeth, H., and P. J. S. Williams, The EISCAT ionospheric radar: The system and its early results, *Q. J. R. Astron. Soc.*, *26*, 478-512, 1985.

Rodger, A. S., S. B. Mende, T. J. Rosenberg, and K. B. Baker, Simultaneous optical and HF radar observations of the ionospheric cusp, *Geophys. Res. Lett.*, *22*, 2045-2048, 1995.

Ruohoniemi, J. M., R. A. Greenwald, K. B. Baker, J.-P. Villain, and M. A. McCready, Drift motions of small-scale irregularities in the high-latitude *F* region: An experimental comparison with plasma drift motions, *J. Geophys. Res.*, *92*, 4553-4564, 1987.

Schunk, R. W., and A. F. Nagy, Electron temperatures in the *F* region of the ionosphere: Theory and observations, *Rev. Geophys.*, *16*, 355-399, 1978.

Starkov, G. V., J. Oskman, M. V. Uspensky, and A. V. Kustov, On the dependence of radar aurora amplitude on ionospheric electron density, *J. Geophys.*, *52*, 49-52, 1983.

Tsunoda, R. T., High-latitude *F* region irregularities: A review and synthesis, *Rev. Geophys.*, *26*, 719-760, 1988.

Vickrey, J. F., and J. D. Kelley, The effects of a conducting *E* layer on classical *F* region cross-field plasma diffusion, *J. Geophys. Res.*, *87*, 4461-4468, 1982.

Villain, J.-P., G. Caudal, and C. Hanuise, A SAFARI-EISCAT comparison between the velocity of *F* region small-scale irregularities and the ion drift, *J. Geophys. Res.*, *90*, 8433-8443, 1985.

Villain, J.-P., R. A. Greenwald, K. B. Baker, and J. M. Ruohoniemi, HF radar observations of *E* region plasma irregularities produced by oblique electron streaming, *J. Geophys. Res.*, *92*, 12,327-12,342, 1987.

Villain, J.-P., C. Hanuise, R. A. Greenwald, K. B. Baker, and J. M. Ruohoniemi, Obliquely propagating ion acoustic waves in the auroral *E* region: Further evidence of irregularity production by field-aligned electron streaming, *J. Geophys. Res.*, *95*, 7833-7846, 1990.

J. A. Davies, M. Lester, and S. E. Milan, Department of Physics and Astronomy, Leicester University, Leicester LE1 7RH, England, U. K. (steve.milan@ion.le.ac.uk)

(Received December 21, 1998; revised June 7, 1999;
accepted June 14, 1999.)